

RESEARCH ARTICLE | JULY 22 2024

# Coupled response of flow-induced vibration and flow-induced rotation of a circular cylinder with a triangular fairing **FREE**

Hongjun Zhu (朱红钧)  ; Hongtao Hao (郝洪涛); Bin Liu (刘斌); Yingmei Li (李英媚)



*Physics of Fluids* 36, 073623 (2024)

<https://doi.org/10.1063/5.0219856>



## Physics of Fluids

Special Topic:  
Selected Papers from the 2023 Non-Newtonian  
Fluid Mechanics Symposium in China

**Submit Today**



# Coupled response of flow-induced vibration and flow-induced rotation of a circular cylinder with a triangular fairing

Cite as: Phys. Fluids **36**, 073623 (2024); doi: 10.1063/5.0219856

Submitted: 21 May 2024 · Accepted: 2 July 2024 ·

Published Online: 22 July 2024



View Online



Export Citation



CrossMark

Hongjun Zhu (朱红钧),<sup>1,a)</sup>  Hongtao Hao (郝洪涛),<sup>1</sup> Bin Liu (刘斌),<sup>2,3</sup> and Yingmei Li (李英媚)<sup>1</sup>

## AFFILIATIONS

<sup>1</sup>State Key Laboratory of Oil and Gas Reservoir Geology and Exploitation, Southwest Petroleum University, Chengdu 610500, China

<sup>2</sup>Faulty of Science, Agriculture and Engineering, Newcastle University, Newcastle Upon Tyne NE1 7RU, United Kingdom

<sup>3</sup>Newcastle Research and Innovation Institute, Newcastle University in Singapore, Singapore 609607, Singapore

<sup>a)</sup> Author to whom correspondence should be addressed: [zhuhj@swpu.edu.cn](mailto:zhuhj@swpu.edu.cn)

## ABSTRACT

In this paper, a numerical simulation investigation is carried out on the coupled response of the flow-induced vibration (FIV) and flow-induced rotation (FIR) of a circular cylinder attached with a triangular fairing at a low Reynolds number of  $Re = 100$ . The primary focus is on the impact of FIR on FIV. The vibration response, hydrodynamic coefficient, vortex shedding mode, and flow field characteristics are examined for the fairings within the vibrational reduced velocity  $U_r$  range of 3–16 with shape angle of  $\alpha = 45^\circ$ ,  $60^\circ$ , and  $90^\circ$ . The results reveal that at low  $U_r$ , all the three considered fairings have a good suppression effect on the FIV. Nevertheless, the galloping response emerges as  $U_r$  increases when  $\alpha = 45^\circ$  and  $60^\circ$ . In contrast, the vibration response of  $90^\circ$  fairing presents a wider lock-in region. The rotatable 2-degree of freedom (2-DoF) fairing has a better performance in the reduction of response amplitude and hydrodynamic coefficients. The 2S (two single vortices) vortex shedding mode mainly occurs in the vortex-induced vibration (VIV) region, while 2S–8S (from two to eight vortices), 2P (two pairs of vortices), 2T (two triplets of vortices), and P + T (a pair of vortices and a triplet of vortices) modes emerge in the galloping branch. Moreover, four modes of wake structures are identified according to the variation of recirculation region and the migration of boundary layer separation point. Finally, the reduced regions of drag, lift, and amplitude are highlighted compared to the bare cylinder.

Published under an exclusive license by AIP Publishing. <https://doi.org/10.1063/5.0219856>

## I. INTRODUCTION

In the context of ongoing advancements in the exploration and exploitation of deepwater hydrocarbon reserves, the operational parameters of offshore drilling and production apparatus are progressively evolving toward heightened complexity. As essential marine drilling and production equipment, risers are very fragile and vulnerable. The vortex-induced vibration (VIV) caused by ocean currents is one of the important factors contributing to the fatigue damage. The VIV is created by alternate shed vortices behind the structures when ocean currents flow past the risers. When the vibration frequency approaches the natural frequency of the structure, the resonance is generated, known as the lock-in phenomenon that exacerbates the fatigue damage.<sup>1</sup> Therefore, many scholars have proposed and developed numerous methods to suppress the VIV. Currently, there are generally two types of control methods. If external energy input is required, it is called active control, and otherwise, it is termed passive control. Typical active control methods include suction,<sup>2,3</sup> synthetic jets,<sup>4,5</sup> and

rotating rods.<sup>6,7</sup> However, the advantages of simple operation, high efficiency, and low cost make passive control more popular. The typical passive control devices include fairing,<sup>8–10</sup> splitter plate,<sup>11–13</sup> helical strake,<sup>14,15</sup> and rough surface.<sup>16,17</sup> Herein, the fairing delays the boundary layer separation point of the riser rearward due to its streamlined shape, effectively suppressing VIV.

Grant and Patterson<sup>8</sup> investigated the VIV suppression using a streamlined fairing. They suggested that it to some extent suppresses the shedding of vortices while effectively reducing amplitude. Wang *et al.*<sup>10</sup> further modified the fairing to a droplet shape and discussed the suppression effect of different tail-angle fairings through numerical simulation. They observed that the best effect was achieved when the tail angle was  $30^\circ$ – $45^\circ$ . Zheng and Wang<sup>18</sup> found that for fairings of different shapes, the smaller characteristic length, the better suppression effect. However, Assi *et al.*<sup>9</sup> showed that both of the splitter plate and the fairing are prone to generate galloping at high reduced velocities. Therefore, many scholars have conducted research on the

galloping response of fairings. Zheng and Wang<sup>19</sup> pointed out that a short-tail fairing can introduce severe galloping oscillation in the region of  $14 < U_r < 19$ , because of the reattachment of the shear layers behind fairings. Xia *et al.*<sup>20</sup> divided the vibration into three branches based on the characteristics of cylinder attached with fairing: the initial branch, the galloping branch, and the lower branch. Subsequently, Xia *et al.*<sup>21</sup> explored the hydrodynamic characteristics of fairing structures under different angles of attack with respect to the incoming flow and found a critical attack angle  $a_c$  using a similar methodology. When the inflow attack angle was greater than  $a_c$ , the fairing arose galloping.

It becomes manifest that the position of the fairing at the posterior segment of the fluid-dynamic object is imperative, owing to their pronounced sensitivity to the orientation of the incident flow. Due to the variable direction of ocean currents, the fairing is greatly refrain from the practical use of VIV suppression in ocean risers. Therefore, a rotatable fairing has been designed in order to better adapt to the ocean current environment. Assi *et al.*<sup>9</sup> investigated the vibration inhibition performance of a freely rotating short-tail fairing. They found that the 60° fairing has the best suppression effect. An experiment on rotatable fairing was conducted by Qi *et al.*<sup>22</sup> It was found that the vibration displacement of marine risers is significantly reduced by the rotatable fairing, and the fairing covering 57% of the riser presents the best performance. Zhu *et al.*<sup>23</sup> discovered through numerical simulation that the reduced velocity  $U_r$  is an important factor affecting the vibration suppression of a free rotating fairing. As  $U_r$  increases, the structure is more prone to instability. The response of a rotating splitter plate is similar to the rotatable fairing. Assi *et al.*<sup>12</sup> experimentally demonstrated that a rotatable splitter plate is effective in reducing the VIV. Through numerical simulation, Tang *et al.*<sup>24</sup> reported that the rotatable splitter plate shows a greater performance in the reduction of hydrodynamic forces and the suppression of vortex shedding as compared to a bare cylinder. In addition, they also proposed three coupled response modes and three reattachment modes of the cylinder-plate body.

Although previous studies have concerned the VIV suppression effect or the unexpected galloping response of circular cylinders attached with fairings, the investigation on the coupled response of the VIV of the cylinder equipped a rotatable fairing is scanty. The interpretation of the interplay between rotation and vibration is not well documented. Therefore, in this work, a comparative analysis is performed on the 1-degree-of-freedom (1-DoF) response (only the cross-flow oscillation) and 2-degree-of-freedom (2-DoF) response (both the rotation and the cross-flow oscillation) of a circular cylinder equipped with a triangular fairing with variable shape angles. The aim is to evaluate the performance of a rotatable fairing and its interaction with the VIV in terms of both response and flow characteristics. A fixed fairing with angle from 45° to 90°<sup>10</sup> or a rotatable fairing with angle from 60° to 120°<sup>9,23</sup> has been proven to have good performance in vibration suppression. For this reason, fairings at angles of 45°, 60°, and 90° are used to further investigate the coupled response of FIV and FIR in this paper.

**II. PROBLEM DESCRIPTION**

The geometric setup is illustrated in Fig. 1. The two side plates of the fairing are tangent to the surface of the cylinder. Therefore, as the angle increases, the intersection points between the fairing and circular cylinder are further back. To conduct a comparable analysis, the same physical materials are used throughout the system. The mass ratio  $m^*$  is set as 2.5, where  $m^* = m/m_d$ , which indicates the ratio of the

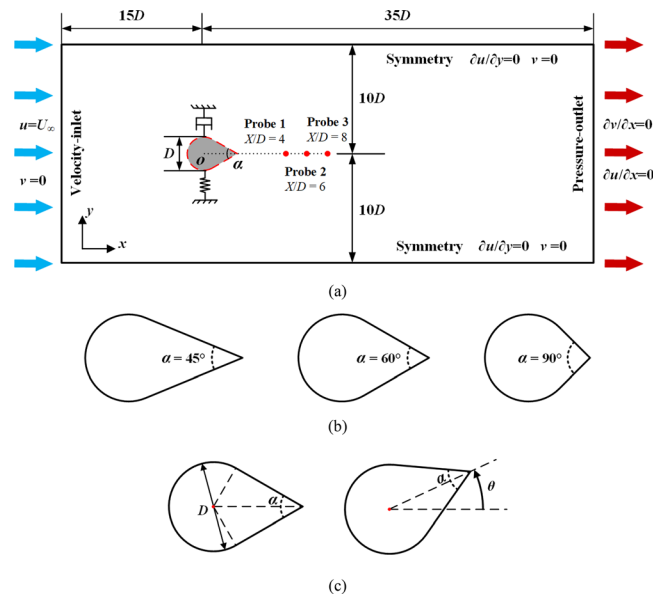


**FIG. 1.** Boundary conditions and geometric model of a circular cylinder with a triangular fairing: (a) boundary conditions; (b) geometric model; and (c) definition of rotation angle  $\theta$ .

structure mass to the displaced mass of fluid. The circular cylinder with diameter of  $D$  attached with the fairing is considered as a mass-spring-damper system with the vibration damping ratio  $\zeta_y = 0.003$  and the rotation damping ratio  $\zeta_\theta = 0.0001$ . The influence of fairing with three shape angles of 45°, 60°, and 90° on the VIV response is

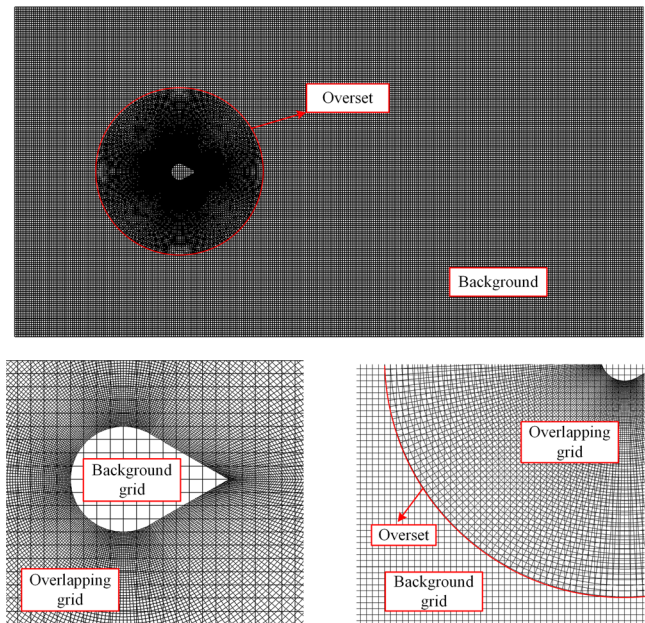


**FIG. 2.** The employed mesh system.

22 July 2024 12:46:17

TABLE I. Convergence analysis on mesh density.

Mesh	Elements	$A_Y/D$	$\theta$ (°)	$C_{D,mean}$	$C_{L,rms}$
M1	38 450	0.514 11	2.6865	1.400 47	0.461 26
M2	63 348	0.493 58 (4.16%)	2.620 19 (2.53%)	1.323 29 (5.83%)	0.437 37 (5.46%)
M3	86 514	0.482 48 (2.30%)	2.595 79 (0.94%)	1.282 97 (3.14%)	0.428 33 (2.11%)
M4	114 562	0.47832 (0.86%)	2.582 34 (0.52%)	1.271 36 (0.91%)	0.424 16 (0.97%)

examined in this work. The numerical simulation is conducted at a fixed of  $Re = 100$  based on the cylinder diameter and the vibrational reduced velocity  $U_r$  range of 3–16. The natural frequency ( $f_n$ ) of the structure in water is defined as

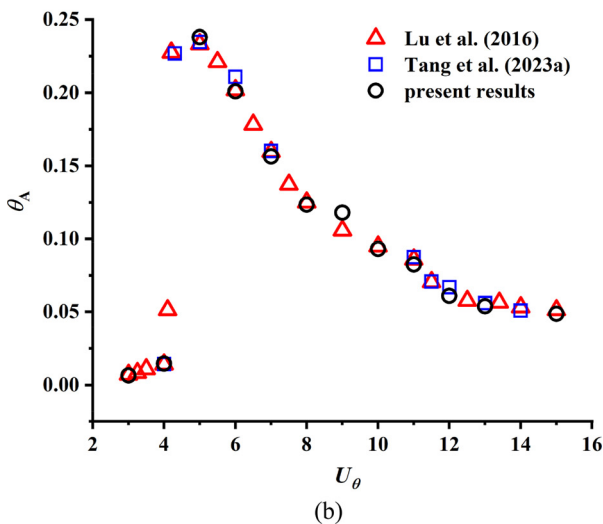
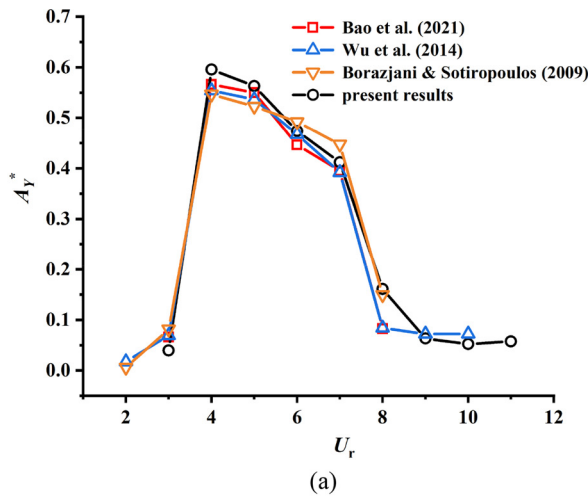


FIG. 3. Model validation: (a) validation of the numerical model for FIV of a circular cylinder and (b) validation of the numerical model for FIR of a circular cylinder with a rigid splitter plate.

TABLE II. Verification of lift and drag coefficients of a bare circular cylinders.

	$C_{D,mean}$	$C_{L,rms}$	$St$
Posdziech and Grundmann <sup>39</sup>	1.325	0.228	0.164
Mittal <sup>40</sup>	1.322	0.226	0.164
Present	1.332	0.228	0.163

$$f_n = \frac{1}{2\pi} \sqrt{\frac{K}{m + m_a}}, \quad (1)$$

where  $K$  is the spring stiffness and  $m_a$  is the added mass,  $m_a = C_a m_d$ , and  $C_a$  is the added mass coefficient defined as<sup>25</sup>

$$C_a = -\frac{8}{nT\rho\pi D^2(2\pi f_Y)^4 A_Y^2} \int_t^{t+nT} f_L(t) Y'' dt, \quad (2)$$

where  $n$  is the number of samples counted for calculation,  $T$  is the oscillation cycle,  $\rho$  is the fluid density,  $f_Y$  is the cross-flow oscillation frequency,  $A_Y$  is the cross-flow amplitude,  $f_L(t)$  is the lift acting on the structure varies over time, and  $Y''$  is the cross-flow acceleration.

As shown in Fig. 1, a rectangular computational domain of  $20D$  (cross-flow direction)  $\times$   $50D$  (in-flow direction) is used for the simulation. Additionally, the distance from the two lateral boundaries to the original point is  $10D$ , resulting in a blockage ratio of 5%.<sup>26,27</sup> It is  $15D$  away from the original point to the entrance boundary. The velocity inlet boundary with  $u = u_\infty$  and  $v = 0$  is applied on the left boundary, where  $u$  is the velocity component in the  $x$ -direction and  $v$  is that in  $y$ -direction. The outlet boundary is  $35D$  away from the original point, imposed with the Newman boundary with velocity gradients of 0 ( $\partial u/\partial x = 0$  and  $\partial v/\partial x = 0$ ). Symmetry boundary conditions with  $\partial u/\partial y = 0$  and  $v = 0$  are imposed on the lateral boundaries. The no-slip condition is imposed on the structure surface. To explore the flow field clearly, three probes are set at  $X/D = 4, 6,$  and  $8$ , behind the structure.

The system is subjected to uniform incoming flow. In addition, the cylinder with fairing can oscillate in the cross-flow direction and rotate passively. The coupled response of FIV and FIR is examined in associated  $U_r$  ranges.

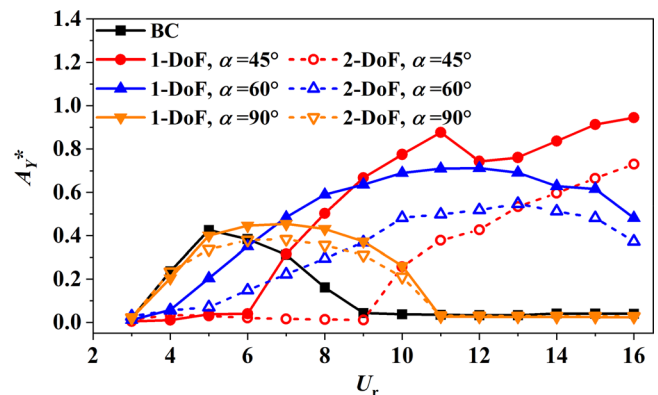


FIG. 4. Comparison of the dimensionless amplitude  $A_Y^*$  between 1-DoF fairing and 2-DoF fairing with different angles, where the result of bare cylinder (BC) is also plotted as baseline denoted.

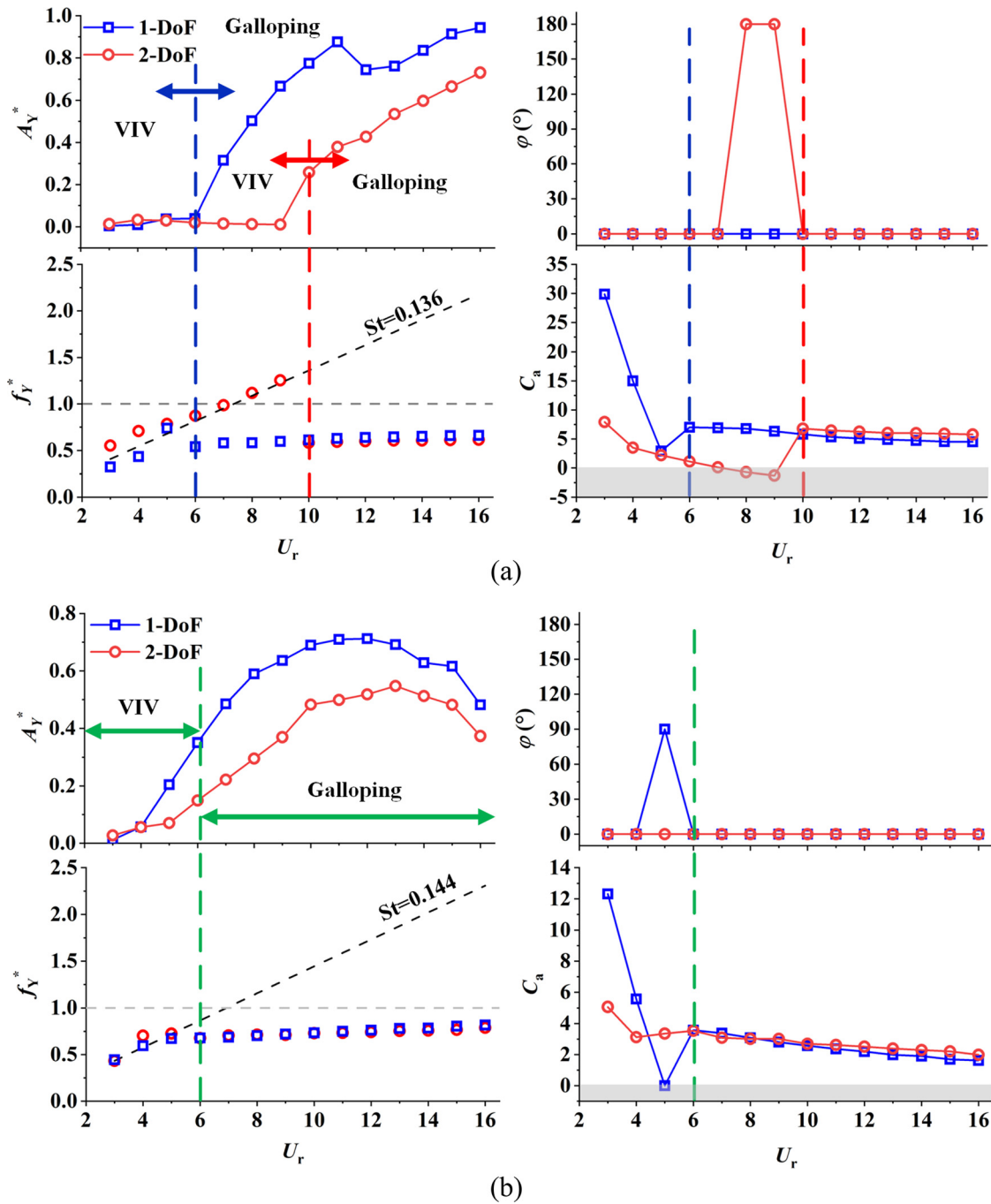


FIG. 5. Comparison of vibration response between the circular cylinders with 1-DoF and 2-DoF fairings: (a)  $\alpha = 45^\circ$ ; (b)  $\alpha = 60^\circ$ ; and (c)  $\alpha = 90^\circ$ .

### III. MATHEMATICAL MODEL

#### A. Governing equations

The incompressible Navier–Stokes equations are used to solve the flow over an elastically mounted circular cylinder with the fairing subjected to the two-dimensional uniform laminar flow. The non-dimensional forms of the continuity and momentum equations are written as<sup>28</sup>

$$\nabla \cdot \mathbf{u}^* = 0, \tag{3}$$

$$\frac{\partial \mathbf{u}^*}{\partial t^*} + (\mathbf{u}^* \cdot \nabla) \mathbf{u}^* = -\nabla p^* + \frac{1}{\text{Re}} \nabla^2 \mathbf{u}^*, \tag{4}$$

where  $\mathbf{u}^*$  is the normalized velocity vector in the Cartesian coordinate system consisting of two components in the  $x$  and  $y$  directions,  $t^*$  is the non-dimensional time, and  $p^*$  is the dimensionless pressure.

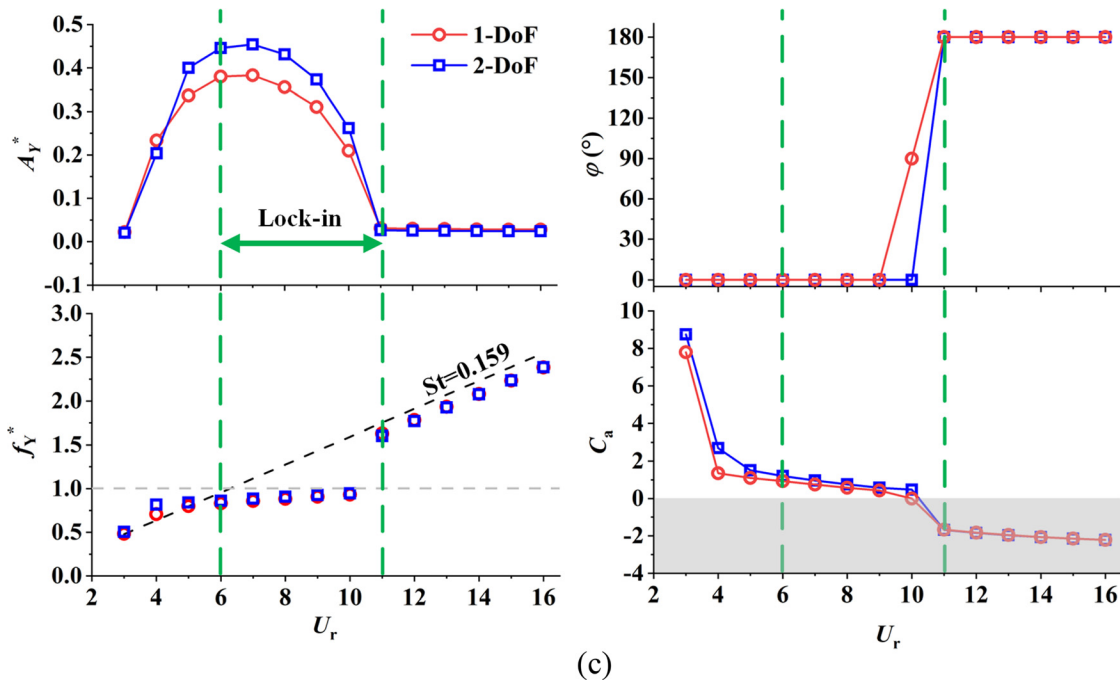


FIG. 5. (Continued).

The fluid force acting on the mass-spring-damping system for the cross-flow vibration is expressed as<sup>29</sup>

$$m\ddot{y} + C_y\dot{y} + K_y y = F_L, \tag{5}$$

where  $m$  is the structural mass,  $y$  is the transverse displacement,  $\dot{y}$  is the transverse velocity,  $\ddot{y}$  is the transverse acceleration,  $C_y$  is the damping constant in vibration system,  $K_y$  is the vibrational stiffness constant that provides elastic resilience of the system, and  $F_L$  is the lift force. The non-dimensional form of Eq. (5) is

$$\ddot{Y} + 2\zeta\left(\frac{2\pi}{U_r}\right)\dot{Y} + \left(\frac{2\pi}{U_r}\right)^2 Y = \frac{C_L}{2m^*}, \tag{6}$$

where  $Y = \frac{y}{D}$  is the non-dimensional displacement,  $\zeta = \frac{C}{2\sqrt{Km}}$  is the vibrational damping ratio,  $U_r = \frac{U}{f_n D}$  is the vibrational reduced velocity,  $f_n$  is the vibrational natural frequency, which varies with  $U_r$ ,  $m^* = \frac{m}{\rho D^2}$  is the mass ratio, and  $C_L = \frac{2F_L}{\rho U D^2}$  is the lift coefficient.

For the 1-DoF rotation response, the governing equation<sup>30,31</sup> is written as

$$I_\theta \ddot{\theta} + C_\theta \dot{\theta} + K_\theta \theta = M_\theta, \tag{7}$$

where  $I_\theta$  is the mass moment of inertia,  $\theta$  (unit: radian) is the rotary angle of the structure around the center of the circle,  $\dot{\theta}$  is the rotary angular velocity,  $\ddot{\theta}$  is the rotary angular acceleration,  $C_\theta$  is the rotary damping constant in the rotation system,  $K_\theta$  is the rotary stiffness constant, and  $M_\theta$  is the moment applied by the fluid to the structure. The non-dimensional form of Eq. (7) is

$$\ddot{\theta} + 2\zeta_\theta \left(\frac{2\pi}{U_\theta}\right) \dot{\theta} + \left(\frac{2\pi}{U_\theta}\right)^2 \theta = \frac{C_M}{2I_\theta^*}, \tag{8}$$

where  $\zeta_\theta = \frac{C_\theta}{2\sqrt{K_\theta I_\theta}}$  is the rotational damping ratio,  $U_\theta = \frac{U}{f_{n\theta} D}$  is the rotational reduced velocity,  $f_{n\theta} = \frac{1}{2\pi} \sqrt{\frac{K_\theta}{I_\theta}}$  is the rotational natural frequency, varying with  $U_\theta$ ,  $C_M = \frac{2M_\theta}{\rho D^2 U^2}$  is the pitching moment coefficient, and  $I_\theta^* = \frac{I_\theta}{\rho D^4}$  is the mass moment of inertia.

The coupled response of FIV and FIR is solved using user-defined functions (UDF) in the ANSYS-FLUENT package. The finite-volume method (FVM) and the coupled algorithm are adopted to discretize and solve the Navier–Stokes equations. The time integration is carried out using the second-order Crank–Nicolson scheme. After solving Eqs. (3) and (4), the pressure and viscous stresses are integrated, and the lift, drag, and moment applied on the structure at each time step are calculated. The fourth-order Runge–Kutta method<sup>32,33</sup> is employed to discretize and solve Eqs. (6) and (8) to get the vibration displacements. After that, the grid is updated and the next time step calculation is carried out. The iteration is carried out until sufficient periodical results are obtained for statistical analysis.

### B. Convergence analysis and computational mesh

In this work, the coupled response is solved using the overlapping mesh method.<sup>34</sup> The quadrilateral meshes are specified to partition the entire computational domain. The overlapping and the background grids near the overset are approximately equal, as illustrated in Fig. 2, to convey the data between overlapping regions and background regions accurately. The finer grids are adopted near structures to

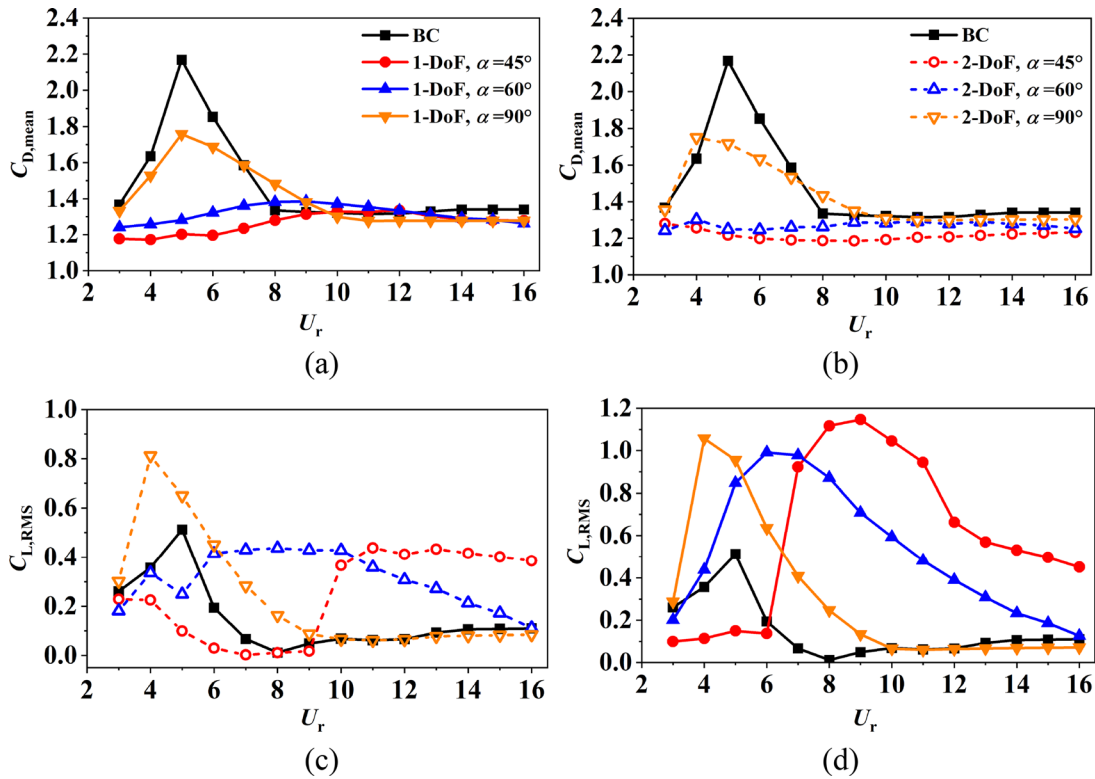


**FIG. 6.** Hydrodynamic coefficients of a cylinder with 1-DoF and 2-DoF fairings: (a) and (b) averaged drag coefficient  $C_{D,\text{mean}}$  for 1-DoF fairing and 2-DoF fairing and (c) and (d) root-mean-squared value of lift coefficient  $C_{L,\text{RMS}}$  for 1-DoF fairing and 2-DoF fairing.

capture the development of boundary layer as well as the changes of hydrodynamic coefficients. In each time step, the flow information in the background domain is first obtained by solving the N-S equations. After that, the data transfer from the background grids to the overlapping grids through the interpolation points. Subsequently, the flow field in the overlapping domain is solved to attain the pressure and shear stress around the structure. The force and torque acting on the cylinder are calculated by integrating the pressure and shear stress. Then, the vibration and rotation response are computed, and the position of the cylinder is updated accordingly. After that, the flow information in the overlapping domain is updated again. Then, the data transfer back to the background grids, and the flow field in the background domain is refreshed. Such an iteration continues until the time meets the requirement.

The grid convergence analysis is performed first for the case of  $\alpha = 60^\circ$  and  $U_r = 10$ . As presented in Table I, there are four grid densities named M1–M4, corresponding to an increase in the number of grids from 38 450 to 114 562. To accurately capture the development of boundary layer, the overlapping region is refined by gradually increasing the nodes on the cylinder perimeter and decreasing the cell expansion ratio from M1 to M4. Accordingly, the height of the first layer of mesh next to the cylinder surface is from  $0.02D$  to  $0.005D$ . In the table,  $A_y/D$  is the normalized transverse amplitude,  $\theta$  is the rotary amplitude,  $C_{D,\text{mean}}$  is the time-averaged drag coefficient, and  $C_{L,\text{rms}}$  is the root-mean-squared (RMS) lift coefficient, defined as

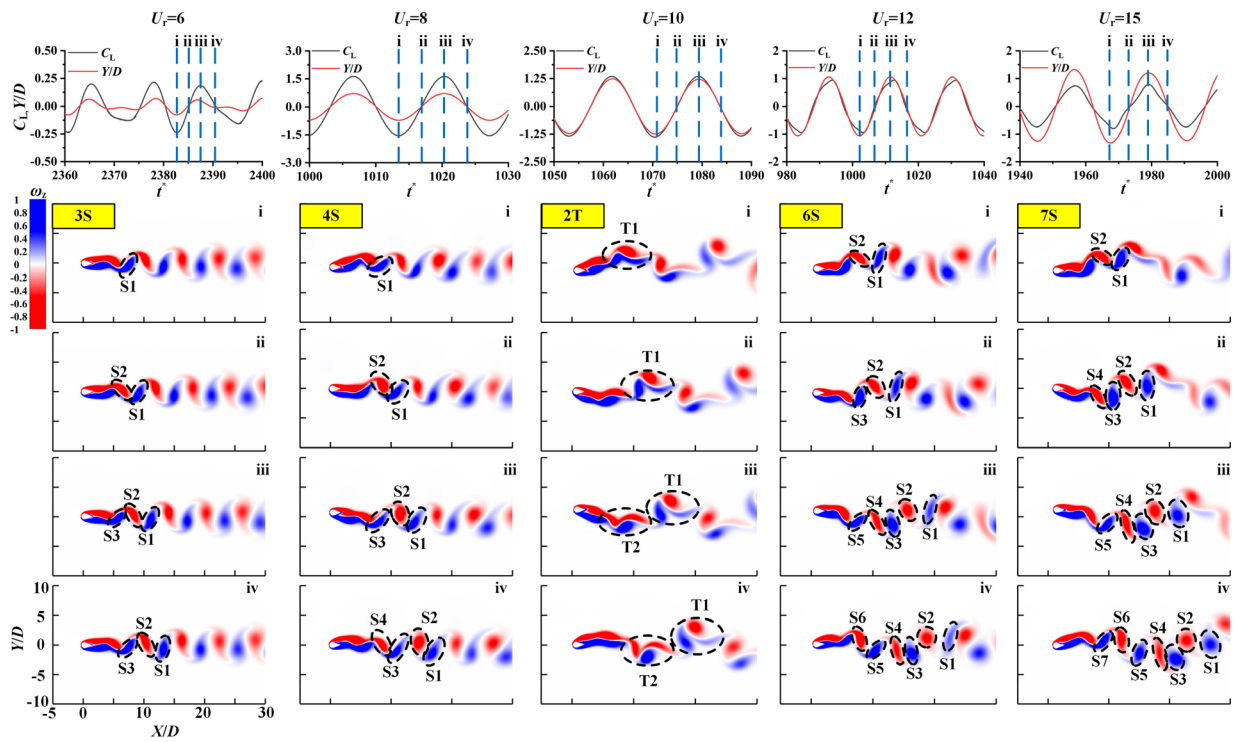
$$C_{D,\text{mean}} = \frac{1}{n} \sum_{i=1}^n \frac{2f_D(t)}{\rho u^2 D}, \quad (9)$$

$$C_{L,\text{RMS}} = \sqrt{\frac{1}{n} \sum_{i=1}^n \left[ \frac{2f_L(t)}{\rho u^2 D} \right]^2}, \quad (10)$$

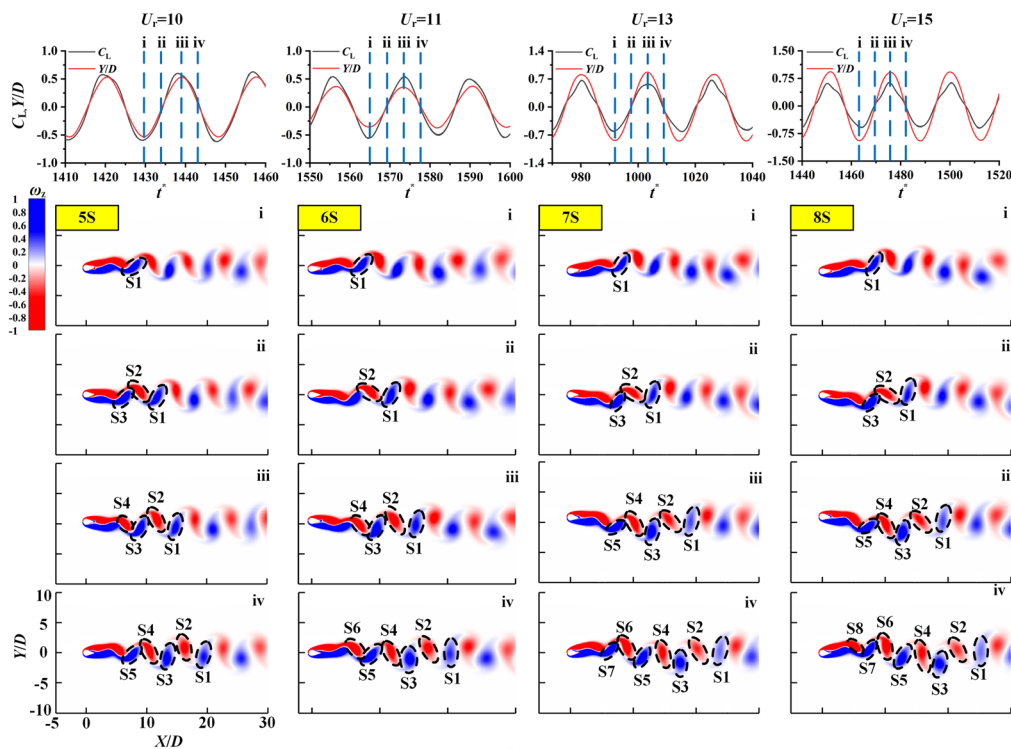
where  $n$  is the number of samples counted for calculation,  $f_D(t)$  is the drag force acting on the cylinder, and  $f_L(t)$  is the lift force acting on the cylinder. As listed in Table I, all differences between M3 and M4 are less than 1%, indicating that further refinement of grids has little impact on the calculation results. Therefore, for a higher computational efficiency, M3 grid density is adopted for the computation, where the height of the first-layer mesh is less than  $0.005D$ . The growth ratio of grid height is kept below 1.02.

### C. Method validation

Currently, the investigations into the flow-induced vibration as well as the flow-induced rotation of fairings at low  $Re$  are relatively scarce. For this reason, two models, the flow-induced vibration of a bare circular cylinder and the flow-induced rotation of a cylinder-plate body, are compared with the results reported in the literature,<sup>35–38</sup> respectively. Figure 3(a) shows the amplitude on different  $U_r$  at  $Re = 100$ ,  $m^* = 2$ , and  $\zeta = 0$ . The absence of a VIV upper branch<sup>1</sup> is due possibly to the greater viscosity force because of a low  $Re$ . However, the initial branch, the lower branch, and the desynchronized



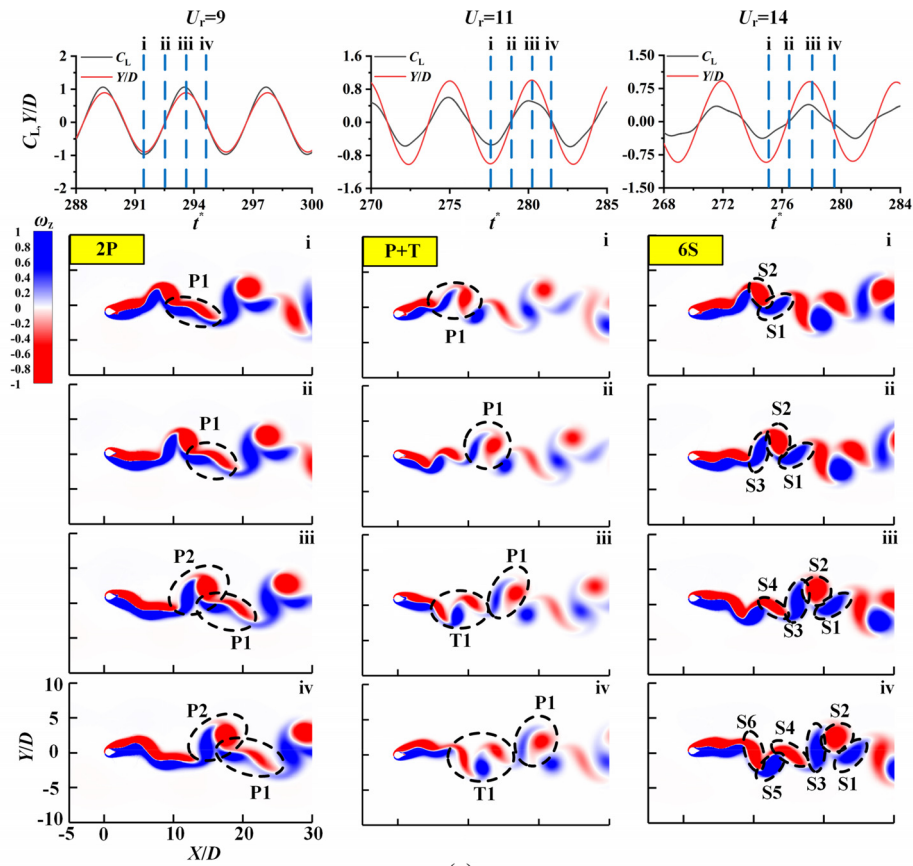
(a)



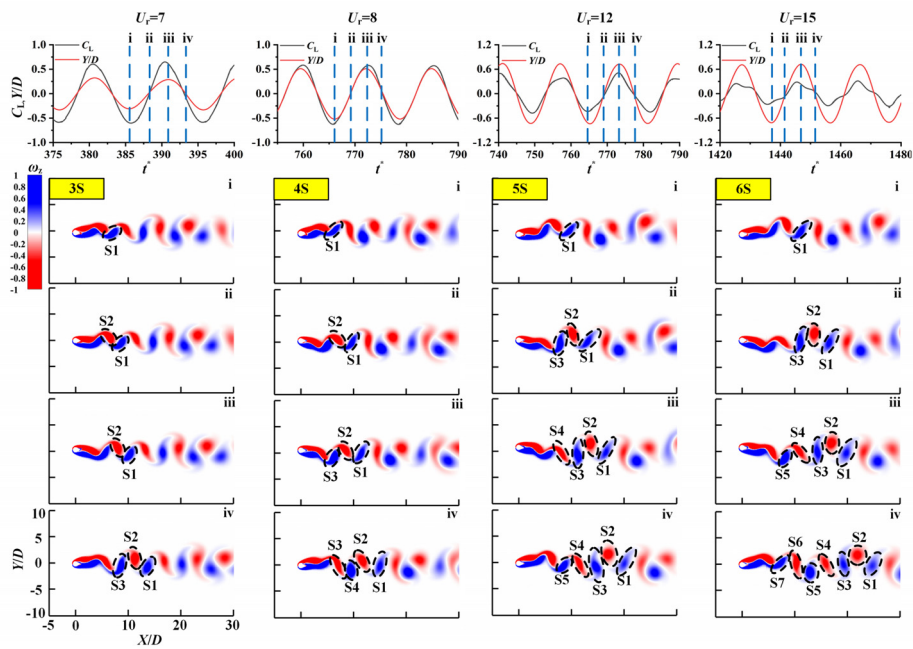
(b)

FIG. 7. Vortex shedding mode: (a) 1-DoF fairing with  $\alpha = 45^\circ$ ; (b) 2-DoF fairing with  $\alpha = 45^\circ$ ; (c) 1-DoF fairing with  $\alpha = 60^\circ$ ; and (d) 2-DoF fairing with  $\alpha = 60^\circ$ .

22 July 2024 12:46:17



(c)



(d)

FIG. 7. (Continued.)

22 July 2024 12:46:17

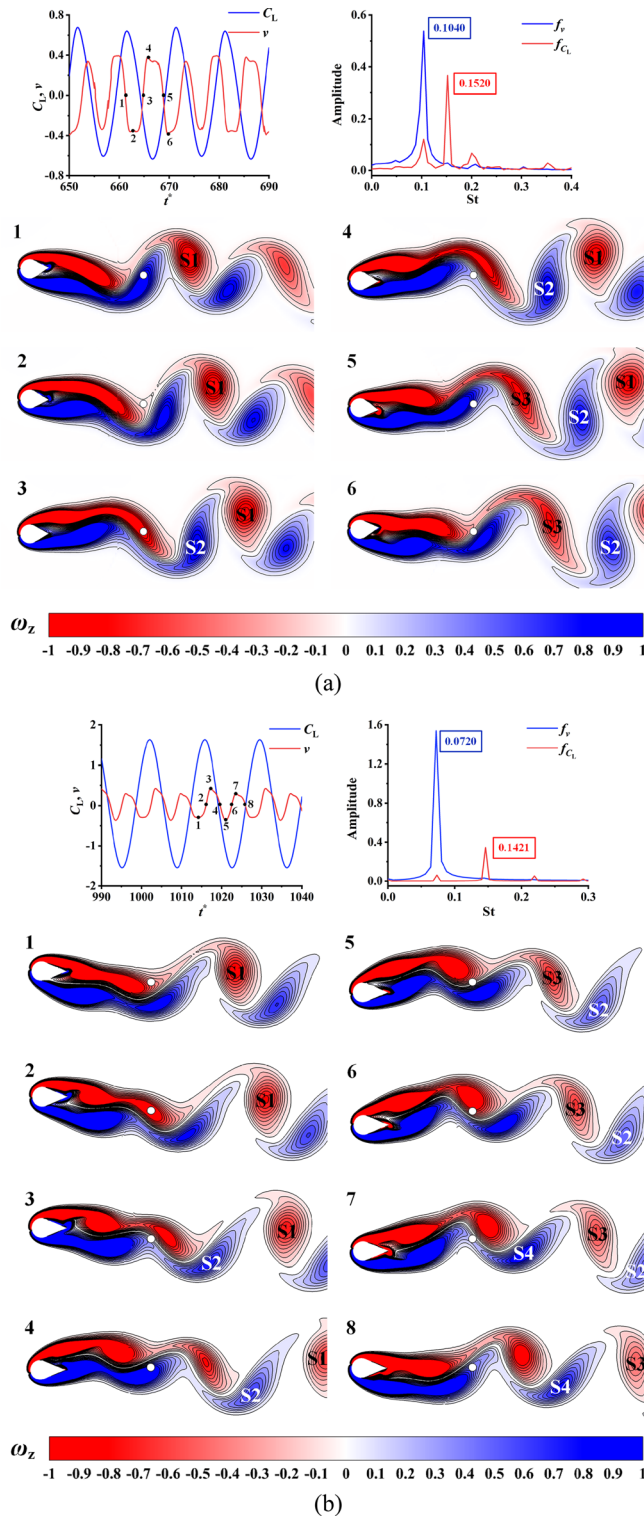


FIG. 8. The relationship of frequency between the lift coefficient and the fluctuation of the transverse velocity at monitoring probe 2 with the vortex shedding process in one cycle: (a) 3S mode and (b) 4S mode.

branch are found. On the other hand, the FIR of a cylinder-plate body at  $Re = 150$ ,  $m^* = 10$ , and  $\zeta_\theta = 0.007$  is also compared, as shown in Fig. 3(b). The relationship between the rotation amplitude  $\theta_A$  and reduced velocity  $U_\theta$  is similar to the VIV response. At  $U_\theta = 5$ ,  $\theta_A$  suddenly increases, presenting a lock-in region. Additionally, the calculation of flow past a bare circular cylinder is also verified. The computed results are listed in Table II. In general, the data obtained from simulations coincide well with the reported results, indicating the validation of numerical method.

## IV. RESULTS AND DISCUSSION

### A. Vibration response

The curve of dimensionless vibration amplitude  $A_Y^* = A_Y/D$  vs  $U_r$  is plotted in Fig. 4. The bare cylinder (BC) exhibits the typical VIV pattern. The initial, lower, and desynchronization branches are observed sequentially as  $U_r$  grows. After attaching a fairing to the cylinder, it has huge influence. For a  $45^\circ$  1-DoF fairing, in low  $U_r$  cases (3–6), it has a good suppression effect on the vibration, where the response amplitude is much lower compared to bare cylinders. However, when  $U_r > 6$ , the vibration amplitude increases sharply. From the vibration frequency ( $f_Y^* = f_Y/f_n$ ) plotted in Fig. 5(a), it is observed that  $f_Y^*$  follows well with the line of  $St = 0.136$  ( $St = f_L D/u$ ,  $f_L$  is the vortex-shedding frequency of the bare cylinder) when  $U_r < 6$ . After that,  $f_Y^*$  becomes less than 1 constantly, evidently indicating the occurrence of galloping.<sup>9,20,41</sup> The transformation from VIV to galloping branch is continuous, with no transitional region. In addition, it is observed that the amplitude decreases at  $U_r = 11$  and quickly recovers thereafter, called “kinks.”<sup>34,42–44</sup> Although the galloping of  $45^\circ$  rotatable 2-DoF fairing occurs at high  $U_r$ , the VIV suppression in the corresponding  $U_r$  range is the best one, as compared to the bare cylinder. The galloping emerges when  $U_r > 10$ , exhibiting a state of high amplitude and low frequency. The phase difference (displacements vs lift coefficients)  $\varphi$  goes through a history of  $0^\circ - 180^\circ - 0^\circ$ , consistent with the positive-negative-positive value of the added mass coefficient  $C_a$ .

As shown in Fig. 4, compared with the  $45^\circ$  fairing, the  $60^\circ$  fairing has a weaker vibration suppression effect at low  $U_r$ , but the increase in amplitude is smaller at high  $U_r$ . Figure 5(b) compares the vibration characteristics of fairings with a shape angle of  $60^\circ$ . Galloping also appears at  $U_r = 6$ , where the vibration frequency does not stay around the level of  $f_Y^* = 1$ . The amplitude significantly decreases as the reduced velocity increases beyond the certain level.<sup>19,18</sup> Compared with the 1-DoF fairing, the 2-DoF fairing with a shape angle of  $45^\circ$  has a smaller displacement amplitude throughout the reduced velocity range, and the same phenomenon was also observed on the  $90^\circ$  fairing. Due to the shorter characteristic length of the  $90^\circ$  fairing, the shape is closer to that of a bare cylinder. Thus, there is no galloping, but rather a VIV with a wider “lock-in” region. Only the rotatable one has a suppressive effect on the VIV at  $U_r = 5$ , and at other  $U_r$ , it actually enhances the vibration.

### B. Hydrodynamic coefficients

The differences in hydrodynamic coefficients between the bare cylinder and it with a fairing are shown in Fig. 6. Both  $C_{D,mean}$  and  $C_{L,RMS}$  of the bare cylinder change with  $U_r$ , increasing initially, then decreasing, and finally stabilizing around a certain value. This variation coincides with the vibration pattern shown in Fig. 4. The drag acting on the cylinder surface is significantly reduced with the introduction of

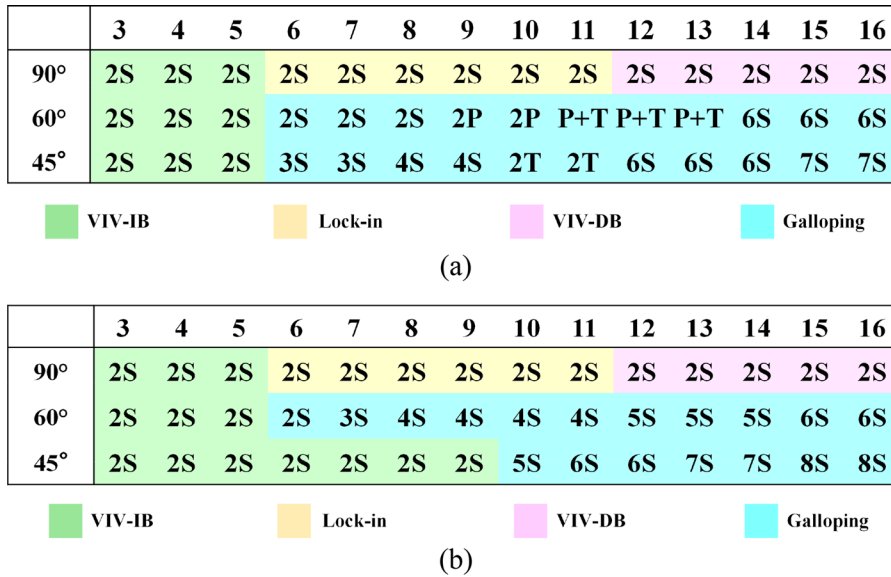


FIG. 9. Division of vortex shedding modes for 1-DoF and 2-DoF fairings: (a) 1-DoF fairing and (b) 2-DoF fairing.

fairing. The smaller the shape angle, the larger the drag reduction. Furthermore, there is no peak of  $C_{D,mean}$  for the fairings with shape angles of 45° and 60°. As seen from Fig. 6(c), the 1-DoF fairing does not have a good effect on the decrease in  $C_{L,RMS}$ .  $C_{L,RMS}$  of the 45° 1-DoF fairing sharp rises at  $U_r = 6$ , resulting in the occurrence of galloping. All three fairings show a tendency of first increasing and then decreasing, and  $U_r$  where the peak value is located gradually increases as the shape angle decreases. For the 2-DoF fairings, as seen in Fig. 6(d), the curve of the 90° fairing is similar to its 1-DoF one, and the 60° fairing has a pit at  $U_r = 5$ . The 45° fairing performs better before the occurrence of galloping. Nevertheless, it has a counterproductive effect on the reduction of  $C_{L,RMS}$  in the  $U_r$  range of 10–16.

**C. Vortex shedding modes**

Figure 7 clearly demonstrates the vortex shedding process of 1-DoF fairing and 2-DoF fairing with different shape angles for one vibration cycle at typical reduced velocities. When  $U_r < 6$ , the cylinder with 45° 1-DoF fairing exhibits the 2S mode (two single vortices), consistent with the finding identified by Williamson and Jauvtis.<sup>45</sup> As  $U_r$  increases, the number of vortices shed in a vibration cycle also rises.

The vortex shedding mode shifts to 3S when  $U_r$  reaches 6. At this time, the vortices are still shedding alternately, but the number of shed vortices on the upper and lower sides of the structure is different in a cycle, as shown in Fig. 7(a). As  $U_r$  increases, multiple pairs of vortices are shed in a vibration cycle. The shed vortices introduce a pressure difference between the upper and lower sides of the structure, resulting in the fluctuation of lift coefficient. As shown in Fig. 7, the lift coefficient frequency is not consistent with the vortex shedding frequency. From Fig. 8, it can be seen that there is a multiple relationship between the lift coefficient frequency and the fluctuation frequency of the transverse velocity at monitoring probe 2. When the vortex shedding mode is 3S, one lift coefficient cycle corresponds to 1.5 fluctuation cycles of the transverse velocity. A similar phenomenon is observed in 4S and other modes. This is possibly attributed to the streamlined shape in the presence of fairing, which pushes downstream the separation point of boundary layers. The vortex shedding modes 4S (four vortices are formed per cycle), 2T (two triplets of vortices), 6S (six vortices are formed per cycle), and 7S (seven vortices are formed per cycle) appear successively along with the increase in  $U_r$  to 16. Compared to the 1-DoF fairing, the 2-DoF fairing maintains 2S mode for a longer time until it shifts to 5S (five vortices are formed per cycle) when  $U_r = 10$ , which is the reason for the lower lift and later occurrence of galloping response. This may be due to the adaptability of the 2-DoF fairing.

For the 60° 1-DoF fairing, as seen in Fig. 7(c), the vortex shedding mode also maintains 2S within the  $U_r$  range of 3–8. The in-phase relationship between the vibration displacement and lift coefficient promotes the gradual enhancement in vibration. The vortex shedding mode shifts to 2P (two pairs of vortices) at  $U_r = 9$ . The P + T mode (a pairs of vortices and a triplets of vortices) appears when  $A_Y^*$  reaches the peak value, and 6S mode exists along with the segment of amplitude decrease. On the contrary, the 2-DoF fairing does not exhibit the complex vortex shedding modes, which gradually shifts from 2S to 6S. Moreover, 1-DoF and 2-DoF fairings with shape angle of 90° always maintain the 2S mode, due possibly to its short characteristic length that has less impact on the separation of shear layers on the cylinder surface.

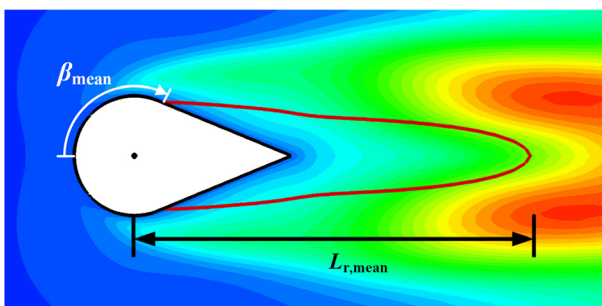


FIG. 10. Schematic diagram of boundary layer separation points angle  $\beta_{mean}$  and recirculation zone length  $L_{r,mean}$ .

22 July 2024 12:46:17

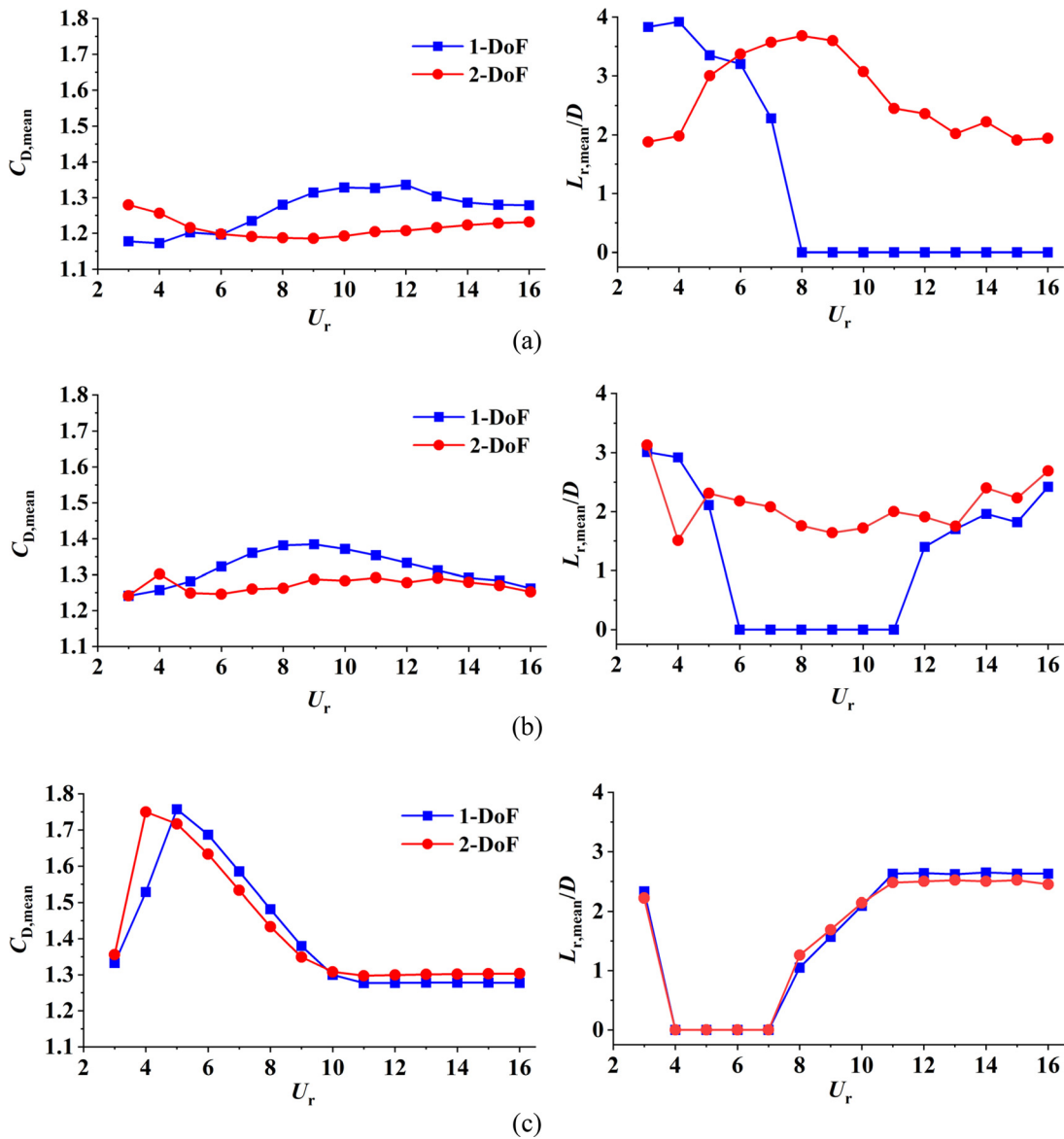


FIG. 11. Comparison of the averaged drag coefficient  $C_{D,mean}$  and of time-averaged recirculation zone length  $L_r/D$ : (a)  $\alpha = 45^\circ$ , (b)  $\alpha = 60^\circ$ , and (c)  $\alpha = 90^\circ$ .

Figure 9 summarizes the division of the vortex shedding modes. Overall, the number of vortices shed in a vibration cycle increases with the increase in reduced velocity for  $60^\circ$  and  $90^\circ$  fairings. At a given  $U_r$ , the smaller the shape angle, the more significant the impact on wake field, resulting in more vortices. The 2S mode only occurs in the VIV branch, and other modes emerge in the galloping branch. The adaptive rotation of fairing contributes to the shed of odd vortices.

#### D. Wake characteristics

Figure 10 illustrates a schematic diagram of the wake flow regime. The zero-value contour of the time-averaged streamwise

velocity is highlighted with solid red line, illustrating the recirculation region.  $L_{r,mean}$  represents the distance from the end point of recirculation region to the center of circular cylinder, suggesting the time-averaged length of recirculation region. The two intersection points of the line with the fairing represent the boundary layer separation points. In this work, the angle from the front stagnation point to the upper boundary layer separation point ( $\beta_{mean}$ ) is used to characterize its variation quantitatively. Figure 11 compares  $L_{r,mean}$  and  $C_{D,mean}$  of the fairing at the same given angle. Overall,  $L_{r,mean}$  shows an opposite trend to  $C_{D,mean}$ . From Figs. 10(a) and 10(b), it can be seen that the adaptability brought about by rotation further reduces  $C_{D,mean}$  and eliminates the appearance of recirculation region in certain situations.

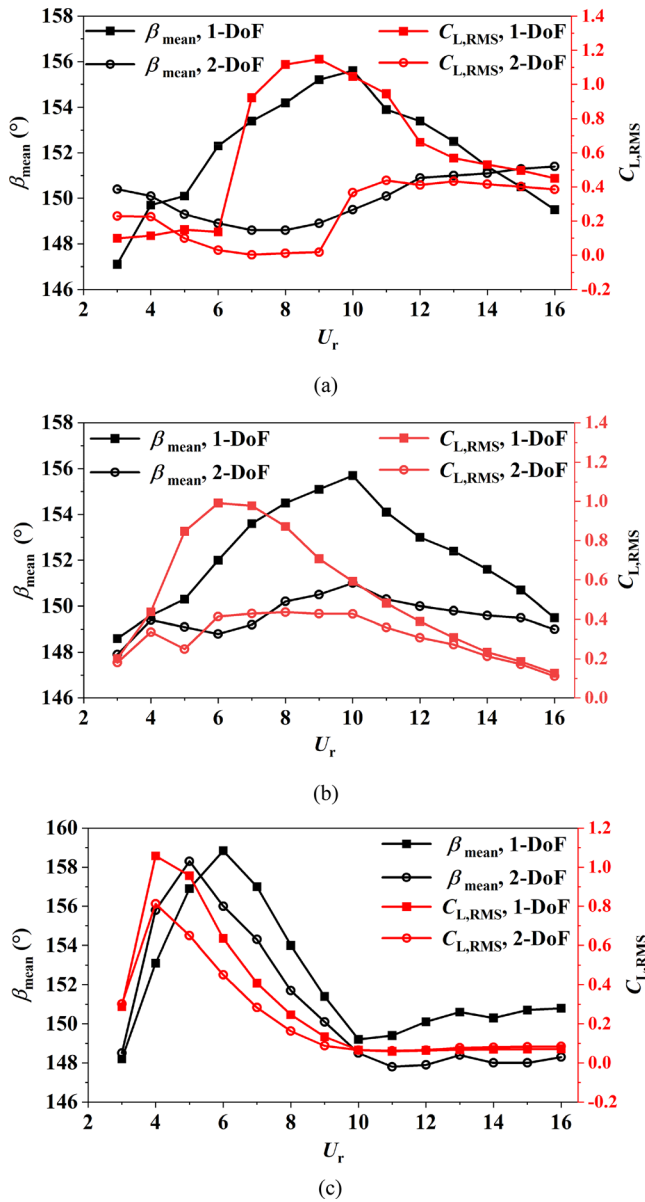


FIG. 12. Comparison of root-mean-squared lift coefficient  $C_{L,RMS}$  and boundary layer separation points angle  $\beta_{mean}$ : (a)  $\alpha = 45^\circ$  (b)  $\alpha = 60^\circ$ , and (c)  $\alpha = 90^\circ$ .

The  $C_{D,mean}$  of the  $45^\circ$  2-DoF fairing has a minimum point, while  $L_r$  has a maximum point. There are no significant peaks in  $L_r$  and  $C_{D,mean}$  for the  $60^\circ$  2-DoF fairing. However, the rotation does not have a good effect on  $90^\circ$  fairing, due to its smaller moment of inertia.

Figure 12 compares the RMS lift coefficient  $C_{L,RMS}$  and the boundary layer separation point angle  $\beta_{mean}$  of 1-DoF and 2-DoF fairings. It is evident that the relationship between  $C_{L,RMS}$  and  $\beta_{mean}$  is proportional in spite of the non-complete synchronous sometimes. Both of them are effectively reduced due to the rotation.

In order to further investigate the influence of fairing, the wake structure is examined. The instantaneous structural posture and the recirculation region for 1-DoF fairings are depicted in Fig. 13. The red lines represent the recirculation region. Based on the evolution, it is classified into four modes: boundary layer separation points on the fairing with continuous recirculation region (F-C), boundary layer separation points on the circular cylinder with continuous recirculation region (C-C), boundary layer separation points and reattached recirculation region switching between the cylinder and fairing (A-R), and boundary layer separation points switching between the cylinder and fairing with broken recirculation region (A-B). An overview is shown in Fig. 13(e). F-C and C-C modes occur in the region with a low amplitude, where the vortices are shed stably. Additionally, the recirculation region does not change significantly over time. As depicted in Fig. 13(d), the fairing presents the maximum displacement at  $t = T/4$  and  $3T/4$ . The tip cuts off the recirculation region into two parts, and the boundary layer separation points swing at the point of tangency, resulting in the A-B mode. Sometimes the recirculation region forms on the upper or lower side of the fairing instead of the cylinder rear. A-B mode is concentrated in the galloping region and lock-in region, and A-R mode is present in the transition region with medium response amplitude.

Figure 14 shows the instantaneous structural posture and the mode partitioning for 2-DoF fairings. Similar to the 1-DoF fairing, the same four modes are observed, but the borderlines change. The 2-DoF fairing results in a smaller amplitude. The tip of the fairing is easier to contact with the contour of  $u = 0$ , resulting in the reattachment of recirculation region. Therefore, the A-R mode dominates the galloping region instead of the A-B mode. Meanwhile, as the initial branch of  $45^\circ$  2-DoF fairing extends, the region of F-F mode also extends accordingly. In contrast, the excessive rotation causes the A-R mode to appear at  $U_r = 3$  and 4. The C-C mode exists in the desynchronization branch for the  $90^\circ$  fairing.

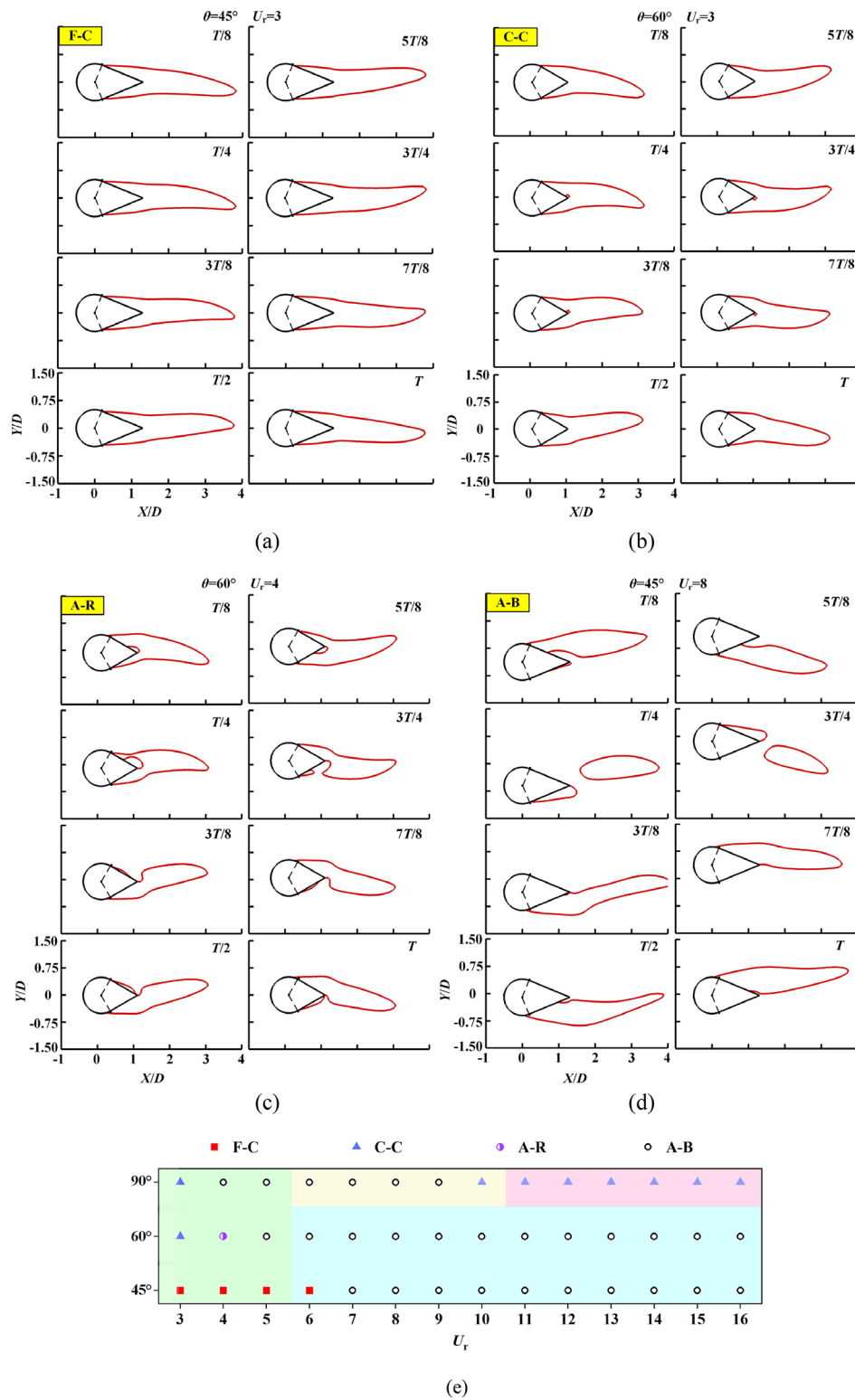
### E. Suppression effect

Figure 15 illustrates the suppression effect of 1-DoF and 2-DoF fairings at different shape angles and reduced velocity. The triangular fairing has a positive impact on  $C_{D,mean}$ , mainly attributed to its streamlined profile. However, the longer characteristic length causes the reattachment of the shear layer, resulting in unstable pulsation of the lift coefficient and the occurrence of galloping. Therefore, the fairing has a negative effect on both vibration suppression and lift reduction in most cases. In the reverse perspective, the fairing could be used as a vibration amplifier for energy harvesting.

### V. CONCLUSIONS

In this paper, we investigate the coupled response of the FIV and FIR of a circular cylinder attached with a triangular fairing with the shape angles of  $\alpha = 45^\circ$ ,  $60^\circ$ , and  $90^\circ$  at  $Re = 100$  in the  $U_r$  range of 3–16 through numerical simulation. The vortex shedding modes and wake structures are identified. The main conclusions are presented as follows:

- (1) The  $45^\circ$  and  $60^\circ$  fairings have a suppression effect on the cylinder VIV at low  $U_r$ . In contrast, at high  $U_r$ , both of them experience galloping response, presenting the negative effect. The



**FIG. 13.** An overview of the wake characteristics for 1-DoF fairings: (a) evolutions of F-C mode; (b) evolutions of A-R mode; (c) evolutions of C-C mode; (d) evolutions of A-B mode; and (e) the summary of wake characteristics.

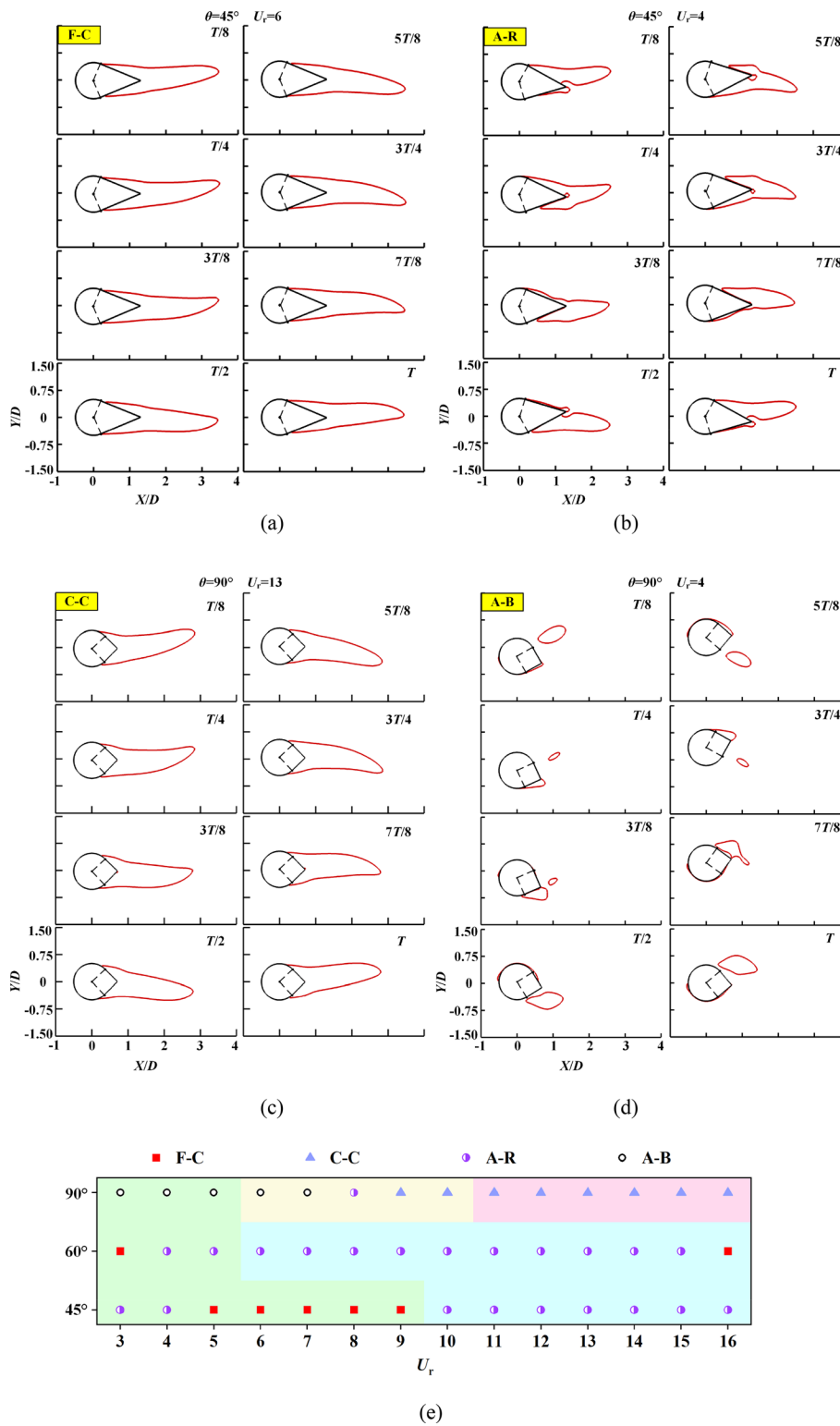


FIG. 14. An overview of the wake characteristics for 2-DoF fairings: (a) evolutions of F-C mode; (b) evolutions of A-R mode; (c) evolutions of C-C mode; (d) evolutions of A-B mode; and (e) the summary of wake characteristics.

22 July 2024 12:46:17

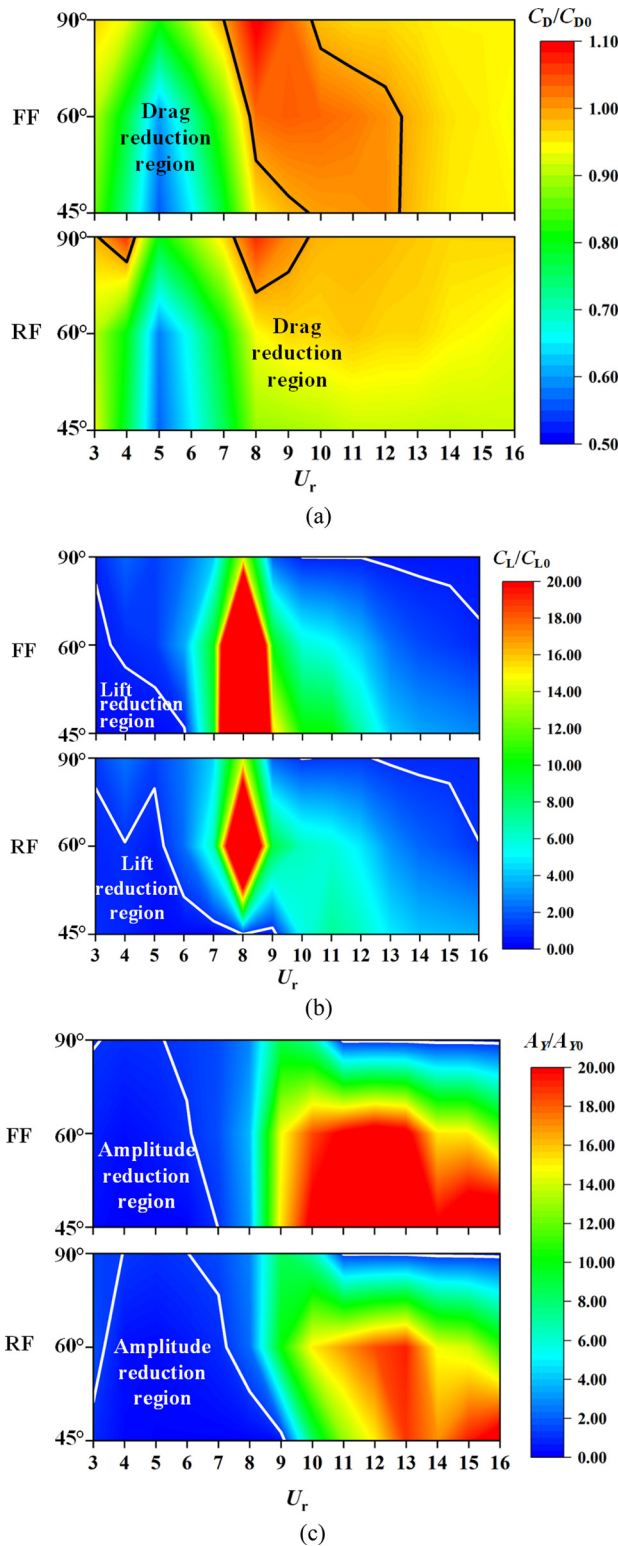


FIG. 15. The reduction regions of drag (a), lift (b), and vibration amplitude (c) compared with the bare cylinder.

- response of 60° fairing exhibits a “kinks” phenomenon at  $U_r = 11$ , while that of 45° fairing continues to increase. The vibration mode of 90° fairing is similar to the bare cylinder. The 2-DoF fairing performs better than the 1-DoF one.
- (2) The fairing effectively reduces the drag coefficient, and the smaller the shape angle, the greater the alleviation. In contrast, for  $C_{L,RMS}$ , the 1-DoF fairing introduces the increases of  $C_{L,RMS}$  in the entire  $U_r$  range. The 45° and 60° 2-DoF fairings only decrease  $C_{L,RMS}$  within a limited  $U_r$  range, and the 90° fairing enlarges the lock-in region.
  - (3) The vortex shedding presents multiple modes. The 2S mode is concentrated in the VIV region. The 2–8S, 2P, P+T, and 2T modes occur in the galloping branch. The number of vortices shed in a vibration cycle increases with the increase in reduced velocity. The instability of vortex shedding causes the irregular pulsation of lift, leading to the galloping.
  - (4) During the vibration process, the boundary layer separation points migrate along the fairing flatbed and cylinder surface, accompanied with the alteration of recirculation bubble shape. Four modes are observed within the entire  $U_r$  range, including the F-C, C-C, A-R, and A-B modes. Galloping branch is dominated by the A-B mode for a 1-DoF fairing, and by the A-R mode for a 2-DoF fairing. F-C mode is concentrated in the initial branch for the 45° fairing, and C-C mode occurs in the desynchronization branch for the 90° fairing.

The two-dimensional simulations are conducted at a low  $Re$  of 100 with a fixed rotation damping ratio. A smaller rotation damping ratio possibly introduces a larger rotational amplitude, and the wake flow evolves to three dimensions when Reynolds number is sufficiently high. Therefore, further extensive studies are required on a broader rotation damping ratio range and higher  $Re$  to conform to engineering requirements, and associated experimental investigations are required for verification.

ACKNOWLEDGMENTS

The research work was supported by the National Natural Science Foundation of China (No. 51979238) and the Sichuan Science and Technology Program (Nos. 2023NSFSC1953 and 2023ZYD0140). The authors appreciate the support from the Offshore Oil and Gas Laboratory at Southwest Petroleum University.

AUTHOR DECLARATIONS

Conflict of Interest

The authors have no conflicts to disclose.

Author Contributions

**Hongjun Zhu:** Conceptualization (equal); Funding acquisition (equal); Methodology (equal); Resources (equal); Supervision (equal); Writing – review & editing (equal). **Hongtao Hao:** Data curation (equal); Formal analysis (equal); Investigation (equal); Validation (equal); Visualization (equal); Writing – original draft (equal). **Bin Liu:** Writing – review & editing (equal). **Yingmei Li:** Investigation (equal).

## DATA AVAILABILITY

The data that support the findings of this study are available from the corresponding author upon reasonable request.

## REFERENCES

- <sup>1</sup>C. H. K. Williamson and R. Govardhan, "Vortex-induced vibrations," *Annu. Rev. Fluid Mech.* **36**, 413–455 (2004).
- <sup>2</sup>J. H. M. Fransson, P. Konieczny, and P. H. Alfredsson, "Flow around a porous cylinder subject to continuous suction or blowing," *J. Fluids Struct.* **19**(8), 1031–1048 (2004).
- <sup>3</sup>W. L. Chen, Y. Cao, H. Li *et al.*, "Numerical investigation of steady suction control of flow around a circular cylinder," *J. Fluids Struct.* **59**, 22–36 (2015).
- <sup>4</sup>M. Amitay and A. Glezer, "Aerodynamic Flow Control Using Synthetic Jet Actuators, Lecture Notes in Control and Information Sciences (LNCIS, 2006), Vol. 330, pp. 45–73.
- <sup>5</sup>L. H. Feng, J. J. Wang, and C. Pan, "Effect of novel synthetic jet on wake vortex shedding modes of a circular cylinder," *J. Fluids Struct.* **26**(6), 900–917 (2010).
- <sup>6</sup>D. Shiels and A. Leonard, "Investigation of a drag reduction on a circular cylinder in rotary oscillation," *J. Fluid Mech.* **431**, 297–322 (2001).
- <sup>7</sup>S. J. Lee and J. Y. Lee, "PIV measurements of the wake behind a rotationally oscillating circular cylinder," *J. Fluids Struct.* **24**, 2–17 (2008).
- <sup>8</sup>R. Grant and D. Patterson, "Riser fairing for reduced drag and vortex suppression," paper presented at the Offshore Technology Conference, Houston, 1977.
- <sup>9</sup>G. R. S. Assi, P. W. Bearman, and M. A. Tognarelli, "On the stability of a free-to-rotate short-tail fairing and a splitter plate as suppressors of vortex-induced vibration," *Ocean Eng.* **92**, 234–244 (2014).
- <sup>10</sup>J. S. Wang, H. X. Zheng, and Z. X. Tian, "Numerical simulation with a TVD-FVM method for circular cylinder wake control by a fairing," *J. Fluids Struct.* **57**, 15–31 (2015).
- <sup>11</sup>C. J. Apelt, G. S. West, and A. A. Szewczyk, "The effects of wake splitter plates on the flow past a circular cylinder in the range of  $10^4 < Re < 10^5$ ," *J. Fluid Mech.* **61**, 187–198 (1973).
- <sup>12</sup>G. R. S. Assi, P. W. Bearman, and N. Kitney, "Low drag solutions for suppressing vortex-induced vibration of circular cylinders," *J. Fluids Struct.* **25**, 666–675 (2009).
- <sup>13</sup>B. Stappenbelt, "Splitter-plate wake stabilization and low aspect ratio cylinder flow induced vibration mitigation," *Int. J. Offshore Polar Eng.* **20** (published online) (2010); available at <https://onpetro.org/IJOPE/article-abstract/35622>.
- <sup>14</sup>I. Korkischko and J. R. Meneghini, "Experimental investigation of flow-induced vibration on isolated and tandem circular cylinders fitted with strakes," *J. Fluids Struct.* **26**, 611–625 (2010).
- <sup>15</sup>Y. Gao, J. D. Yang, Y. M. Xiong, M. H. Wang, and D. Lu, "VIV response of a long flexible riser fitted with different helical strake coverages in uniform and linearly sheared currents," *Ships Offshore Struct.* **12**, 575–590 (2015).
- <sup>16</sup>B. Zhou, X. K. Wang, W. Guo, W. M. Gho, and S. K. Tan, "Experimental study on flow past a circular cylinder with rough surface," *Ocean Eng.* **109**, 7–13 (2015).
- <sup>17</sup>H. J. Zhu, Y. M. Li, H. T. Hao, M. M. Alam, T. M. Zhou, and T. Tang, "Experimental investigation on the vortex-induced vibration of a circular cylinder partially covered with moss," *Ocean Res.* **298**, 117198 (2024).
- <sup>18</sup>H. X. Zheng and J. S. Wang, "Galopping oscillation of a circular cylinder firmly combined with different shaped fairing devices," *J. Fluids Struct.* **77**, 182–195 (2018).
- <sup>19</sup>H. X. Zheng and J. S. Wang, "Numerical study of galopping oscillation of a two-dimensional circular cylinder attached with fixed fairing device," *Ocean Eng.* **130**, 274–283 (2017).
- <sup>20</sup>X. Xia, L. J. Zhou, Y. Lv, and Z. W. Wang, "Numerical investigation of two degree-of-freedom galopping oscillation of a cylinder attached with fixed fairing device," *Ocean Eng.* **240**, 109971 (2021).
- <sup>21</sup>X. Xia, H. Y. Zeng, Z. W. Wang, L. J. Zhou, and C. M. Liu, "Galopping of two-dimensional section of a marine riser attached with fairing under different inflow angles," *Ocean Eng.* **260**, 112055 (2022).
- <sup>22</sup>X. L. Qi, D. G. Zhang, H. Y. Guo, and Y. X. Chen, "The fairing arrangement for vortex induced vibration suppression effect in soliton current," *J. Coastal Res.* **103**, 293–298 (2020).
- <sup>23</sup>H. J. Zhu, Z. H. Liao, Y. Gao, and Y. Zhao, "Numerical evaluation of the suppression effect of a free-to-rotate triangular fairing on the vortex-induced vibration of a circular cylinder," *Appl. Math. Modell.* **52**, 709–730 (2017).
- <sup>24</sup>T. Tang, H. J. Zhu, Q. Xiao, Q. Y. Chen, J. W. Zhong, Y. M. Li, and T. M. Zhou, "Coupled responses of the flow-induced vibration and flow-induced rotation of a rigid cylinder-plate body," *Ocean Eng.* **286**, 115709 (2023).
- <sup>25</sup>K. Vikestad, J. K. Vandiver, and C. M. Larsen, "Added mass and oscillation frequency for a circular cylinder subjected to vortex-induced vibration and external disturbance," *J. Fluids Struct.* **14**, 1071–1088 (2000).
- <sup>26</sup>G. S. West and C. J. Apelt, "The effect of tunnel blockage and aspect ratio on the mean flow past a circular cylinder with Reynolds numbers between 104 and 105," *J. Fluid Mech.* **114**, 361–377 (1982).
- <sup>27</sup>Q. Zheng and M. M. Alam, "Intrinsic features of flow past three square prisms in side-by-side arrangement," *J. Fluid Mech.* **826**, 996–1033 (2017).
- <sup>28</sup>R. Bhatt and M. M. Alam, "Vibrations of a square cylinder submerged in a wake," *J. Fluid Mech.* **853**, 301–332 (2018).
- <sup>29</sup>Y. Gao, H. J. Zhu, X. Y. Zhou, M. M. Alam, T. M. Zhou, and T. Tang, "Wake flow structure and hydrodynamic characteristics of flow around a C-shaped cylinder with variable attack angle at low Reynolds numbers," *Phys. Fluids.* **36**, 013607 (2023).
- <sup>30</sup>T. Tang, H. J. Zhu, Q. Y. Chen, G. M. Li, and T. M. Zhou, "CFD analysis of flow-induced rotation of a circular cylinder with a detached rear splitter plate in laminar flow," *Ocean Eng.* **266**, 112703 (2022).
- <sup>31</sup>I. Robertson, L. Li, S. J. Sherwin, and P. W. Bearman, "A numerical study of rotational and transverse galopping rectangular bodies," *J. Fluids Struct.* **17**, 681–699 (2003).
- <sup>32</sup>H. J. Zhu, T. Tang, Y. Gao, T. M. Zhou, and J. L. Wang, "Flow-induced vibration of a trapezoidal cylinder placed at typical flow orientations," *J. Fluids Struct.* **103**, 103291 (2021).
- <sup>33</sup>T. Tang, H. J. Zhu, G. M. Li, and J. Z. Song, "Comparative study of the flow-induced vibration of a circular cylinder attached with front and/or rear splitter plates at a low Reynolds number of 120," *J. Offshore Mech. Arct. Eng.* **145**, 011903 (2023b).
- <sup>34</sup>H. J. Zhu, Y. M. Li, J. W. Zhong, and T. M. Zhou, "Numerical investigation on the effect of bionic fish swimming on the vortex-induced vibration of a tandemly arranged circular cylinder," *Phys. Fluids* **36**, 037146 (2024).
- <sup>35</sup>Y. Bao, D. Zhou, and J. Tu, "Flow interference between a stationary cylinder and an elastically mounted cylinder arranged in proximity," *J. Fluids Struct.* **27**, 1425–1446 (2021).
- <sup>36</sup>J. Wu, C. Shu, and N. Zhao, "Numerical investigation of vortex-induced vibration of a circular cylinder with a hinged flat plate," *Phys. Fluids* **26**, 063601 (2014).
- <sup>37</sup>I. Borazjani and F. Sotiropoulos, "Vortex-induced vibrations of two cylinders in tandem arrangement in the proximity-wake interference region," *J. Fluid Mech.* **621**, 321–364 (2009).
- <sup>38</sup>L. Lu, X. L. Guo, G. Q. Tang, M. M. Liu, C. Q. Chen, and Z. H. Xie, "Numerical investigation of flow-induced rotary oscillation of circular cylinder with rigid splitter plate," *Phys. Fluids* **28**, 093604 (2016).
- <sup>39</sup>O. Posdziech and R. Grundmann, "Electromagnetic control of seawater flow around circular cylinders," *Eur. J. Mech., B: Fluids* **20**(2), 255–274 (2001).
- <sup>40</sup>S. Mittal, "Control of flow past bluff bodies using rotating control cylinders," *J. Fluids Struct.* **15**, 291–326 (2001).
- <sup>41</sup>H. J. Zhu, G. M. Li, and J. L. Wang, "Flow-induced vibration of a circular cylinder with splitter plates placed upstream and downstream individually and simultaneously," *Appl. Ocean Res.* **97**, 102084 (2020).
- <sup>42</sup>T. Miyata, M. Miyazaki, and H. Yamada, "Pressure distribution measurements for wing induced vibrations of box girder bridges," *J. Wind Eng. Ind. Aerodyn.* **14**, 223–234 (1983).
- <sup>43</sup>P. W. Bearman, I. S. Gartshore, D. J. Maull, and G. V. Parkinson, "Experiments on flow-induced vibration of a square-section cylinder," *J. Fluids Struct.* **1**, 19–34 (1987).
- <sup>44</sup>C. Mannini, A. M. Marra, and G. Bartoli, "VIV-galopping instability of rectangular cylinders: Review and experiments," *J. Wind Eng. Ind. Aerodyn.* **132**, 109–124 (2014).
- <sup>45</sup>C. H. K. Williamson and N. Jauvtis, "A high-amplitude 2T mode of vortex-induced vibration for a light body in XY motion," *Eur. J. Mech., B: Fluids* **23**, 107–114 (2004).